International Journal of Heat and Mass Transfer 52 (2009) 5608–5623

Contents lists available at ScienceDirect

International Journal of Heat and Mass Transfer

journal homepage: www.elsevier.com/locate/ijhmt

Non-linear dynamical analyses of transient surface temperature fluctuations during subcooled pool boiling on a horizontal disk

Vijaykumar Sathyamurthi, Debjyoti Banerjee *

Department of Mechanical Engineering, Texas A&M University, 3123, TAMU, College Station, TX 77843-3123, USA

A R T I C L E I N F O

Article history:
Received 20 December 2007
Received in revised form 1 May 2009
Available online 27 July 2009

Keywords:
Boiling
Thin film thermocouples
Correlation dimension
Critical heat flux
Leidenfrost point
Mutual information
Chaos

A B S T R A C T

The class of dynamics in pool boiling on a large-size heater is assessed under subcooled pool boiling conditions. Transient surface temperature measurements are obtained using surface micro-machined K-type thin film thermocouples (TFT) in 10 °C subcooled pool boiling experiments on a 62.23 mm diameter silicon wafer using PF-5060 as the test liquid. Surface temperature data is obtained at each steady state condition to generate the boiling curve. The fraction of false-nearest neighbors, recurrence plots and space–time separation plots are obtained using the TISEAN package. The correlation dimension is then estimated from the re-constructed phase space data using a naïve algorithm. The correlation dimension varies from ~11.2 to 11.5 near onset of nucleate boiling (ONB), to ~7–10 in fully developed nucleate boiling (FDNB) ~7–9 near critical heat flux (CHF) condition, and from ~6.6 to 7.7 in film boiling. False-nearest neighbor estimates and recurrence plots show that nucleate boiling may be dominated by statistical processes near ONB and in partial nucleate boiling (PNB). In contrast, FDNB, CHF and film boiling seem chaotic and governed by deterministic processes.

1. Introduction

Pool boiling heat transfer is influenced by a number of transport processes with coupled parameters [1]. Understanding the dynamics of underlying transport mechanisms is vital to its applicability to new practical applications such as electronic chip cooling [2]. Extensive theoretical and experimental studies have been carried out to determine the factors influencing nucleation site activation and bubble dynamics [3]. Processes affecting the boiling processes include heater surface characteristics, the type of fluid and the spatio-temporal variations of solid–liquid–vapor interfaces [4]. Earlier efforts [5] in this field employed spatially and temporally averaged data in developing models to predict the heat fluxes. The importance of measuring surface temperatures with adequate spatial and temporal resolution in pool boiling systems has recently gained emphasis [6,7]. Micro-fabrication techniques can provide the necessary spatio-temporal resolution needed for a thorough understanding of the phase change process. Recently, Myers et al. [8] used a micro-heater and a high-speed camera to obtain spatio-temporally resolved temperature and heat flux measurements in pool boiling of FC-72.

Harris and Johnson in [9] reported the concept of thin film thermocouples in the 1930s. Marshall et al. [10] studied various combinations of thermocouple elements. Bullis [11], Assanis and Friedmann [12], Debey et al. [13], Tian et al. [14], and Laugier [15] used thin film thermocouples (TFT) for various surface temperature measurements. TFT possess excellent high frequency response [16] due to its low thermal inertia. They can be fabricated at locations where a wire-bead thermocouple would interfere in the normal functioning of the object. Furthermore, the minimal thermal inertia and small feature size leads to a reduced distortion of the temperature and velocity fields in its vicinity. Ahn et al. [17] used thin film thermocouples to measure the surface temperature fluctuations in film boiling in order to verify the presence of cold spots. Lüttich and others [6,7], recently used micro-machined TFT to estimate the surface temperature and heat flux fluctuations in pool boiling. However, the TFT was covered with a sputtered layer of gold 0.001 mm in thickness leading once again to an indirect estimation of surface temperature and heat fluxes.

In the past decade alternative approaches to understanding pool boiling mechanisms has emerged. It has been suggested that a pool boiling system is dissipative and therefore chaotic [18–21]. Dynamical systems that are chaotic have strange attractors. Strange attractors are those patterns that characterize the final state of dissipative system [22]. The characterization of geometrical aspects of these strange attractors serves as a measure of the number of parameters required to describe the system. Strange attractors are found to possess fractal geometry and hence are characterized by fractal dimensions, which may or may not be a whole number (positive). High-dimensional experimental systems are known to possess low dimensional attractors [23]. Grassberger and Procaccia [24] suggested the use of a measure closely related

---

* Corresponding author. Tel.: +1 979 845 4500; fax: +1 979 845 3081.
E-mail address: dbanerjee@tamu.edu (D. Banerjee).

0017-9310/$ - see front matter © 2009 Elsevier Ltd. All rights reserved.
doi:10.1016/j.ijheatmasstransfer.2009.06.023

Nomenclature

A	area (m^2)
$\widehat{C}$	correlation sum (–)
d	embedding dimension (–)
D	attractor dimension (–)
g	acceleration due to gravity (m/s^2)
I	mutual information (bits)
k	thermal conductivity (W/m-K)
m	vectors in a embedding dimension (–)
n	index of pairs of vertically aligned thermocouples in heating block (–)
N	total number of time-series data points (–)
$P(a,b)$	joint probability density for measurements resulting in a and b (–)
q	average heat in the axial direction (W)
$\overline{q''}$	mean heat flux assuming 1-D conduction (W/cm^2)
r	radius of ball centered at $\bar{z}_i$/space scale (–)
t	time index (–)
T	temperature (°C)
$U(\cdot)$	unit step function (–)
x	distance between the two vertically aligned thermocouples (m)
$\bar{z}$	vectors in a given phase space
Greek symbols	
Δ	difference (–)
ε	neighborhood/space scale (–)
ν	correlation dimension (–)
ω	relative uncertainty in the quantity denoted by the subscript (–)
σ	information theoretic entropy (–)
τ	delay (–)
Subscripts	
Cu	copper heating block (–)
F	fractal dimension (–)
i	index of thermocouple pair when used with T else index of points in a given phase space
j, k	indices of thermocouples located within the copper heating cylinder
max	maximum
opt	optimal
q	uncertainty in Heat flux
v	vapor phase
w	wall/silicon wafer surface

to fractal dimension and information theoretic entropy. This measure is now commonly called the "correlation dimension" and is easier to estimate than other dimensional measures. The relation between the three measures is:

$$\nu \leqslant \sigma \leqslant D_F \tag{1}$$

In order to evaluate the aforementioned dimensional measures, a high frequency measurement of one variable is sufficient provided "adequate" number of noise-free data is available [25]. This is made possible in case of a pool boiling system by use of thin film thermocouples to measure surface temperature fluctuations.

The correlation dimensions of saturated pool boiling of water over short wires were investigated by Shoji et al. [26]. The size of the wires used in that study was of the order of the size of bubbles and thus the classical pool boiling curve was not obtained. Furthermore, temperature fluctuations of the order of 70 K were observed in film boiling. The surface temperatures fluctuations were estimated by measuring the fluctuation in the resistance of the wire using a specially designed electrical circuit. The Fourier spectra was broad banded and positive. Positive Lyapunov exponents were obtained. Conclusions were drawn regarding the underlying determinism using the broadband Fourier spectrum and fractal dimensions.

In [19], the thermo-hydraulic interaction between two nucleating sites was studied. The distance between the sites was varied and the thermal fluctuations were recorded. It was found that the temperature fluctuations became more complex for certain site spacing. For site spacing below a particular value, thermal and hydrodynamic interactions were significant. Consequently, the attractor had a "wool-ball" shape indicative of a dimensionality greater than three. No such effort has been made to quantify the correlation dimensions of attractors in subcooled pool boiling on a large-size heater with multiple nucleation sites.

Since the publication of [26], a number of different techniques to estimate dimensions and establish the existence of determinism have been established. Qualitative techniques such as false-nearest neighbor tests and visual techniques such as recurrence plots and space–time separation plots have been established in the chaos literature [27]. The objectives of this study are:

(i) To demonstrate the suitability of TFT to acquire surface temperature data in pool boiling.
(ii) To demonstrate the use of recently published techniques for non-linear time-series analysis.
(iii) To determine class of dynamics (deterministic/stochastic, periodic/chaotic, etc.) in subcooled pool boiling on a large-size heater.

The study of dynamics of surface temperature fluctuations in pool boiling is crucial for emerging applications such as electronics cooling wherein local hotspots are present and need to be avoided. The confirmed presence of deterministic chaos or non-linear determinism will aid in the development of predictive models for surface temperature fluctuations and by extension hotspots. Furthermore, feedback control systems can be developed to limit the surface temperatures based on these models. A procedure similar to that outlined in Refs. [26,28] is used to estimate the correlation dimensions of attractors in this study.

2. Micro-fabrication and packaging of TFT

The K-type TFT used in this study are fabricated in an eight step process consisting of (i) first layer photolithography, (ii) oxygen-plasma cleaning, (iii) chromel deposition, (iv) lift off, (v) second layer photolithography, (vi) oxygen-plasma cleaning, (vii) alumel deposition, and (viii) lift off.

(A) Photolithography: The positive photoresist (Shipley 1827) is spin coated on the 3″ silicon wafers using a SCS P6204 non-programmable spin coater at 3000 rpm for 60 s. A photo-mask bearing the desired pattern is mounted on a Quintel Q400 MA mask aligner during the photolithography step. The photoresist is exposed to UV-light for 20 s. The wafer is immersed in MF-319 developer solution for 78 s to remove the exposed photoresist.

(B) Oxygen-plasma cleaning and metal deposition: The patterned silicon wafer is cleaned using a reactive ion etcher for 10 s prior to metal deposition. This enables better adhesion of the patterned metal layers to the silicon wafer substrate.

K-Type thermocouples consisting of chromel (+) and alumel (−) junction are surface micro-machined on the silicon wafer. Chromel and alumel wires obtained from Omega Inc. are used as targets. The chromel wires are stripped of their sheathing, cut manually to ~2 cm in length and placed in a graphite crucible liner within the E-beam Metal evaporator (CHA, Model: SEC 600). A 10-nm thick adhesion layer of chromium is first deposited on the wafer followed by deposition of ~250 nm of chromel.

(C) Lift-off: "Lift-off" process is then used to remove the unwanted metal deposited on the wafer leaving behind only the desired pattern. Fig. 1(A)–(C) depicts the design of the chromel and alumel patterns. Fig. 1(A) shows the chromel pattern and Fig. 1(B) the alumel pattern. Fig. 1(C) shows a schematic image of the TFT and Fig. 1(D) shows a digital image of the packaged wafer without the beaded thermocouples.

All the three processes described above are repeated for the deposition of the alumel layer. The width of both chromel and alumel layers is less than 50 μm and the pitch of the thermocouples is 200 μm at the junction. The deposition thickness of each metal is ~250 nm. An array of 5 × 2 thermocouples is fabricated in an area of 800 μm × 200 μm.

(D) Material characterization: Due to the very nature of physical vapor deposition process and difficulties in evaporating alloys (resulting from differences in the partial pressures of constituents), the composition of the TFT is not same as the thermocouple wire. A material surface characterization is performed using X-ray photoelectron spectroscopy (XPS). The alumel layer contains 81.2–84.3% nickel and 15.7–18.8% aluminum by mass. The chromel layer contains 78.5–80.8% nickel and 19.2–21.5% chromium. The XPS can characterize a material surface (~1–10 nm depth) and not the bulk volume. Thus, the composition may not be homogeneous in each material layer. Therefore, a calibration step is essential before the TFT are ready for use in experiments.

(E) Packaging: Sheathed wires of chromel and alumel are attached to the bond pads using adhesive bonding. A steel-epoxy adhesive (Manufacturer: J-B weld, Product Name: JB Weld) is then applied to facilitate adhesion of the junction of the lead wires to their respective bond pads. The bond pads are not in the proximity of the actual TFT junctions and do not affect the thermocouple signals.

3. Description of experimental apparatus and procedure

3.1. Description of apparatus

The experimental apparatus consists of (i) a viewing chamber containing, (a) a heat exchanger coil, (b) a copper block with embedded cartridge heaters and sheathed thermocouples, (c) a steel jacket surrounding the copper block, (d) the test surface

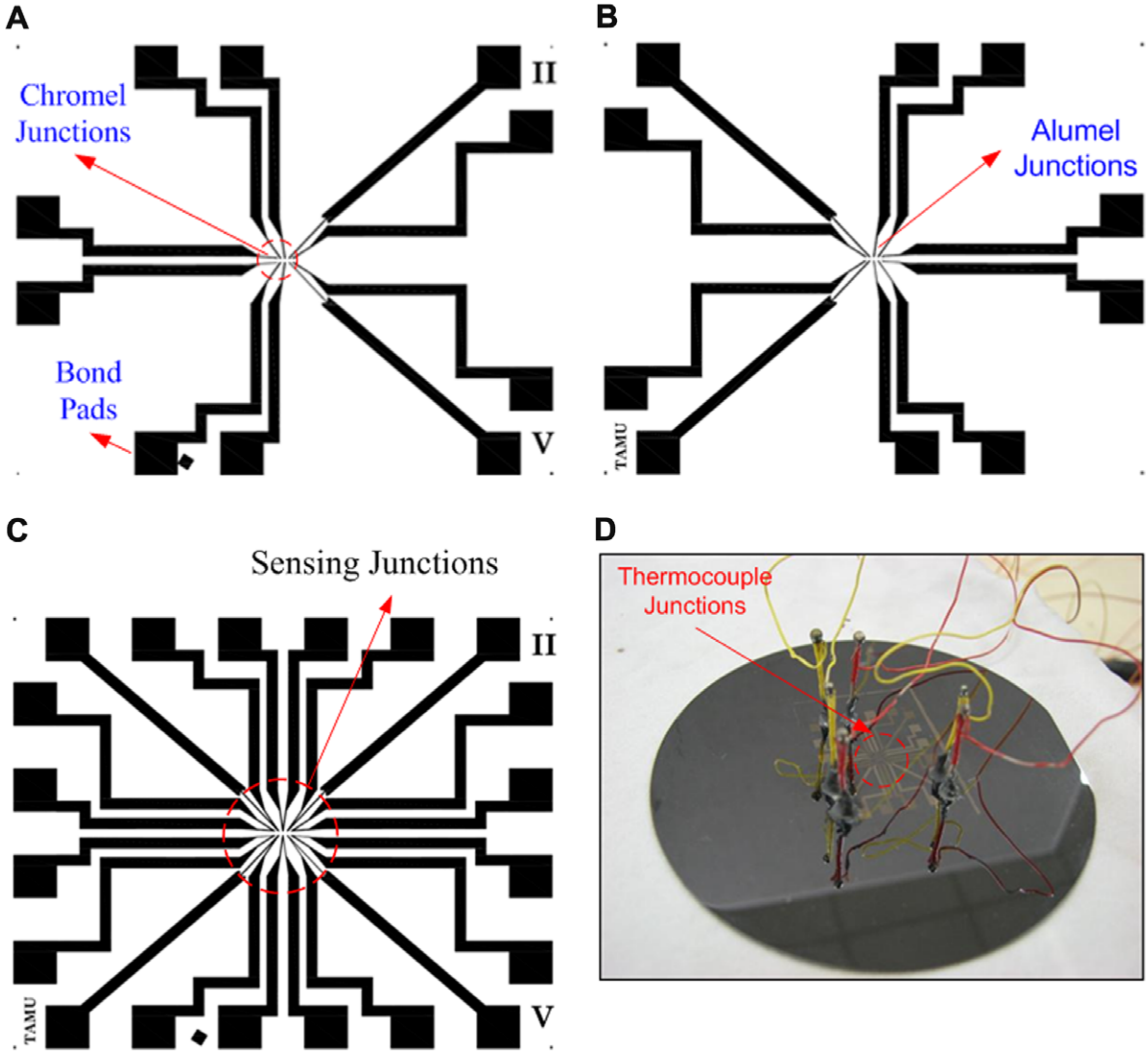

Fig. 1. Depict the layout of the TFT. (A) Layout of the chromel layer; (B) the layout of the alumel layer; (C) the final layout of the TFT; and (D) a packaged TFT without beaded thermocouples.

mounted on the copper block; (ii) a circulator/chiller/constant temperature bath for maintaining the test liquid at a constant temperature (Manufacturer: Polyscience, Division of Preston Industries Inc., Model: Circulator 9612) with a cooling capacity of 700 W at 20 °C; (iii) a data acquisition system; (iv) an AC power supply; and (v) the test surface. Fig. 2(A) depicts a schematic of the entire experimental setup. Fig. 2(B) depicts a schematic of the test section after mounting the test surface. Fig. 2(C) shows the copper block with the cartridge heaters and some of the embedded thermocouples. The sealed viewing chamber has a cast iron frame with three

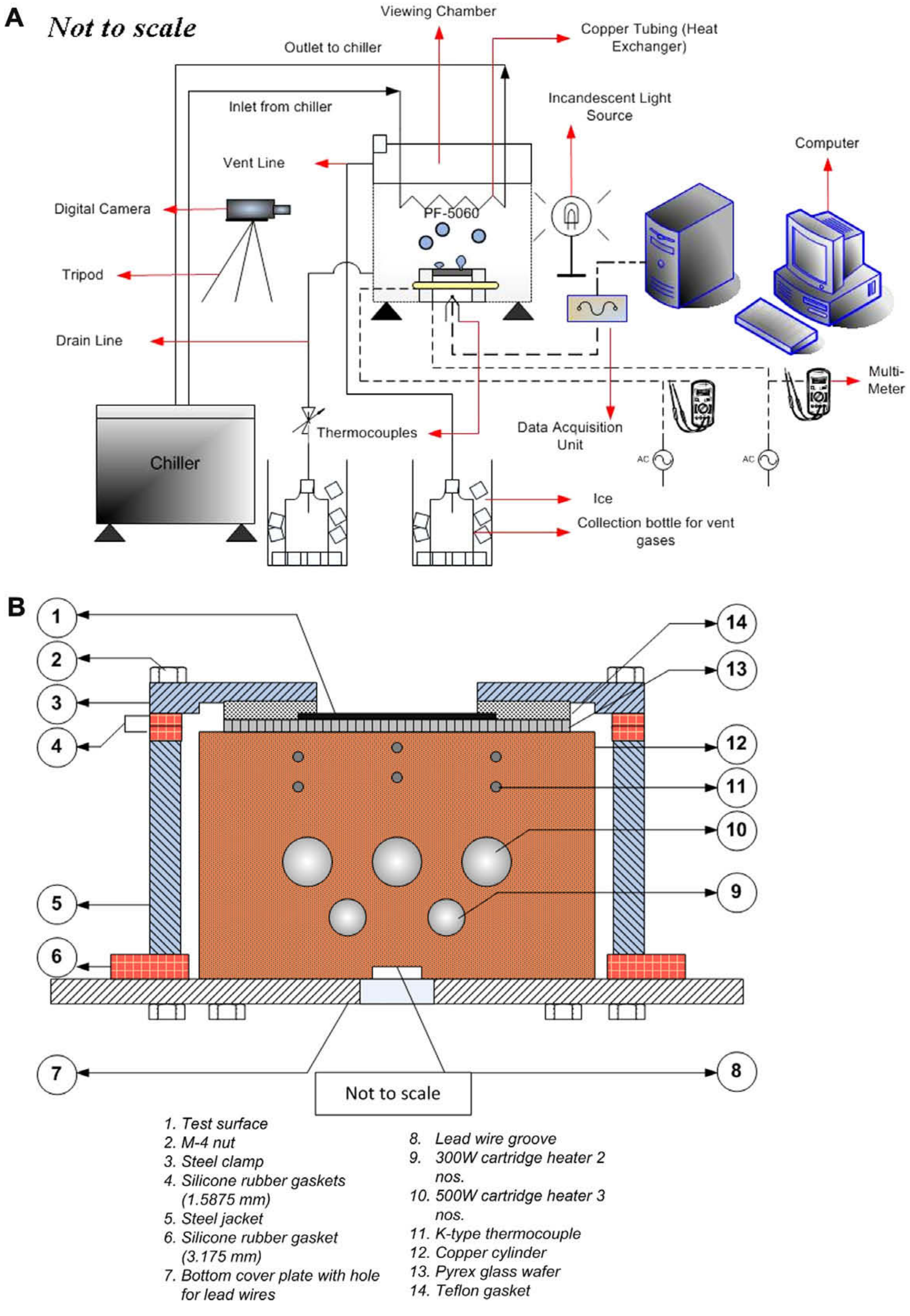

Fig. 2. (A) Schematic of experimental setup; (B) schematic of test section; and (C) schematic of copper heating cylinder.

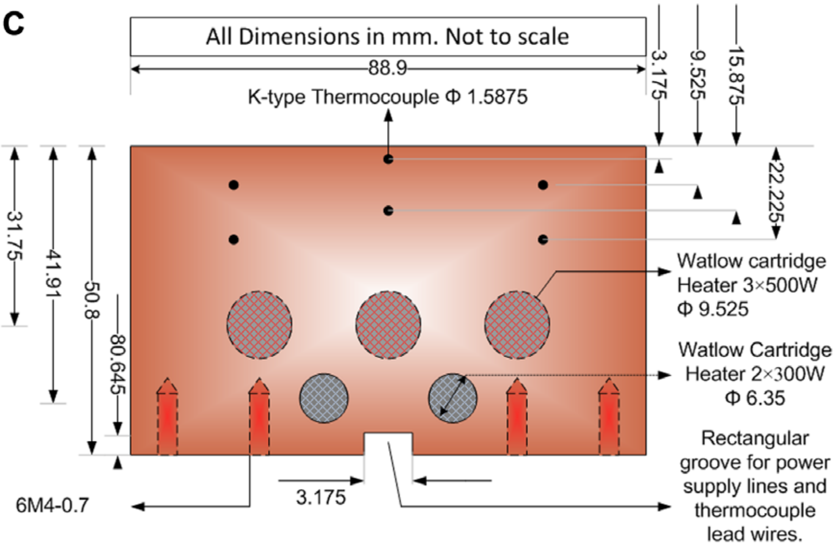

Fig. 2 (*continued*)

viewing windows made of Pyrex. It houses a copper block (∅ 88.9 mm × 50.8 mm), a cooling coil for condensing the vapors and maintaining a constant subcooling level of the liquid. The ends of the cooling coil are connected to an external constant temperature bath. The copper block has five Watlow® cartridge heaters inserted at precise locations in recesses made for the same purpose with a combined power rating of 2.1 kW. Twelve K-type (Manufacturer: Omega®) thermocouples are placed at different radial and axial positions within the copper block for estimating the temperatures and hence the flux of heat. The copper block is surrounded by a steel jacket placed concentric to it resulting in an insulating air gap of ~6.35 mm. The bottom of the viewing chamber is insulated using Styrofoam insulation. The viewing chamber is mounted on four legs and the leg heights are adjusted to level the boiling surface in a horizontal orientation. The wires connecting the thermocouples and cartridge heaters are accessed from the bottom of the chamber, which are then connected to the data acquisition system and power supply, respectively. Additionally, three thermocouples are placed at different heights within the viewing chamber for monitoring the liquid temperature. Two thermocouples are placed ~1–2 cm above the steel clamp. The difference in temperature between the two thermocouples is ~0.5 °C. One thermocouple is placed ~5 cm from the surface in vicinity of the cooling coil. The viewing chamber is covered with a cover plate on the top during the tests. The pressure within the viewing chamber is maintained constant at 1 atm. during the tests. A vent pipe is installed in the chamber side-wall which allows the vapors formed during the test to pass through it, down to the vapor collection bottle placed underneath the test section in an ice bath. The ice bath facilitates the condensation of the vapors generated within the chamber during the test.

3.2. The experimental procedure

The pool boiling experiments comprise of the degassing step and the subsequent data acquisition step. The experimental duration varies between 20 and 30 h. The entire test procedure is outlined below.

3.2.1. Test surface installation

A layer of Dow Corning® 340, silicone heat sink compound is applied on the top horizontal surface of the copper block. A 75 mm Pyrex wafer is placed on the copper block. A silicon wafer is placed on the Pyrex wafer after applying another layer of heat sink compound on the former. A Teflon sheet is fixed to the underside of the steel clamp using silicon glue. The steel clamp has an outer diameter of 114.3 mm with a concentric circular opening, 62.23 mm in diameter, which exposes the silicon wafer to the test liquid. The exposed wafer area is ~30.44 cm^2. This value of exposed area is used for the heat flux estimations. After curing, the clamp is fixed to the jacket using screws. The clamp is tightened uniformly using a torque wrench (torque 3–4.4 N-m). The Teflon sheet underneath the clamp prevents any damage to the wafer surface.

3.2.2. Leak test

A leak test is performed using de-ionized (DI) water after the test surface installation. If a leak is detected the screws are tightened gradually. The apparatus is allowed to dry overnight after the test.

3.2.3. Calibration of TFT

There are inherent difficulties in calibrating TFT [29]. In these tests, the TFT are calibrated in a two-step procedure. The first step involves calibrating a sheathed, beaded, K-type thermocouple by dipping the sensing junction in a constant temperature bath. An NIST partial immersion thermometer with 0.1 °C graduations is used as a reference. The temperature is recorded by the beaded thermocouple (in LABVIEW) and the NIST thermometer once the liquid bath reaches steady state. Calibration of the beaded thermocouple in this manner eliminates bias errors (removable bias) that may have arisen due to welding. Other sources of bias comprise of the following: temperature stability of the constant temperature bath (~0.01 °C), the limited precision of the DAQ system (~0.005 °C) and limited resolution of the NIST thermometer (~0.05 °C). These persist after calibration and contribute to the total uncertainty of the beaded thermocouple. The resulting uncertainty in temperature of the beaded thermocouple due to the aforementioned bias errors and precision errors is approximately constant (~0.15 °C, with a 95% confidence interval) in magnitude. The resulting uncertainty in calibration curves (due to least squares fit) of the beaded thermocouple is not evaluated, as it does not contribute significantly towards the uncertainty.

The two calibrated K-type wire-bead thermocouples are placed on opposite sides of the TFT. The thermocouples are cemented on the silicon wafer containing the packaged TFT using the steel-epoxy adhesive. One beaded thermocouple is located ~10 mm along the transverse direction and ~22.5 mm longitudinally from the sensing junctions of the TFT located at the center of the wafer. Another beaded thermocouple is located a distance ~16.25 mm horizontally, aligned longitudinally to the TFT sensing junctions opposite to the other beaded thermocouple. The calibration curve results in a linear curve fit which expresses the relation between the thermocouple temperature and the NIST thermometer temperature, i.e. the actual temperature. This linear relation is then fed into the LABVIEW program. Thus, the corrected/actual temperature is obtained in real-time as the software computes the equivalent NIST reading corresponding to the thermocouple reading using the curve fit in the second step of the calibration process.

The packaged wafer is installed within the chamber as outlined above. The second calibration step is conducted within the viewing chamber in air. The top of the viewing chamber is closed during this calibration to prevent any external convection currents from affecting the results. The only bulk motion that occurs is due to natural convection currents arising from the density differential within the viewing chamber which do not cause significant spatial temperature differences. The copper heating block is heated and the temperature measurements from the beaded thermocouple and the TFT are acquired in real-time using LABVIEW. Once steady state is attained corresponding to each power setting, the temperature is recorded. Four to five steady state points encompassing the entire operational range of the TFT are obtained in this manner. Using these steady state readings of the calibrated beaded thermocouples and the TFT, a linear calibration curve is obtained between the TFT and the calibrated beaded thermocouple and by extension the NIST thermometer. Prior to the pool boiling tests, the slope and the intercept for the linear fit are fed into the corresponding TFT channel in LABVIEW software. The uncertainty in surface temperature measurements in the pool boiling curve is thus ~0.2 °C, after factoring in the random fluctuations. It must be noted that the calibration procedure does not affect the transient response of the TFT in any manner and serves to eliminate bias and relate the TFT signal to the reference standard, i.e. the NIST thermometer. Further details of the calibration process can be obtained in Refs. [16,17].

3.2.4. Degassing step

The cooling coil is lowered into the viewing chamber and top steel plate is clamped using screws, on the viewing chamber framework. Prior to start of the actual experiment a degassing step is performed. This is done to remove the trapped gases within the test fluid and to prevent premature nucleation. The bulk test fluid is heated to its boiling point and maintained at that temperature for 20 min. The test fluid in this case is PF-5060 (Manufacturer: 3M Co., boiling point: 56 °C). PF-5060 has high oxygen solubility ~60%. Earlier studies [30] have shown that the dissolved oxygen content of PF-5060 does not fall below 39% despite several days of degassing. While the dissolved oxygen content is not measured in the present study, it is reasonable to expect a ~45% dissolved oxygen content.

3.2.5. Data acquisition

After degassing, depending upon the nature of experiments (saturation or subcooling) the cooling coil is either placed above the test fluid (saturation experiments) or immersed (subcooling experiments) in the test fluid.

The temperature of the chilling unit is fixed to achieve a desired temperature level of the test fluid. The power supply to the tubular guard heater is disconnected (for subcooling cases). The guard heater is used for saturation cases to maintain the liquid at its saturation temperature for the lower wall superheats. Power supply to the cartridge heaters is modulated by the variac. The system is allowed to reach steady state for each power setting. The temperature of the test fluid is carefully monitored in LABVIEW® and adjustments to the chiller temperature level are made accordingly during the time taken to reach steady state. The temperatures within the copper block are also monitored continuously in LABVIEW®. Once steady state is achieved, the DAQ system is used to record the thermocouple readings for periods ranging from two minutes at a rate of 200 Hz to ~30 s at a rate of 1 kHz. Data is also recorded at sampling frequencies of 400 Hz, 500 Hz, 600 Hz, and 800 Hz for varying time-periods such that the total file size is similar in all cases. The temperature readings are used to evaluate the heat flux and wall superheats. These are then used to construct the boiling curve (Fig. 4) for PF-5060. The current and voltage supplied to the cartridge heaters are recorded manually using the clamp type ammeter and multi-meter, respectively. In addition, the chiller temperature is recorded periodically. A Canon® S3 IS digital camera is used to capture digital images after steady state conditions are reached. The power supplied is increased in steps of 3 or 5 V and the aforementioned data acquisition procedure is repeated. Further details of the experimental setup, procedure can be found in Ahn et al. [17]. Critical heat flux (CHF) condition is reached when the total power supplied to the heater is ~300 W. A slight increase in power at this stage results in the surface being covered by a vapor film that in turn results in a significant increase in the wall superheat. Once the vapor blanket covers the surface, the voltage and hence temperature is reduced maintain temperatures below ~250 °C. After steady state is reached, the data is recorded and the power supply is lowered further in steps of ~3 V with data being

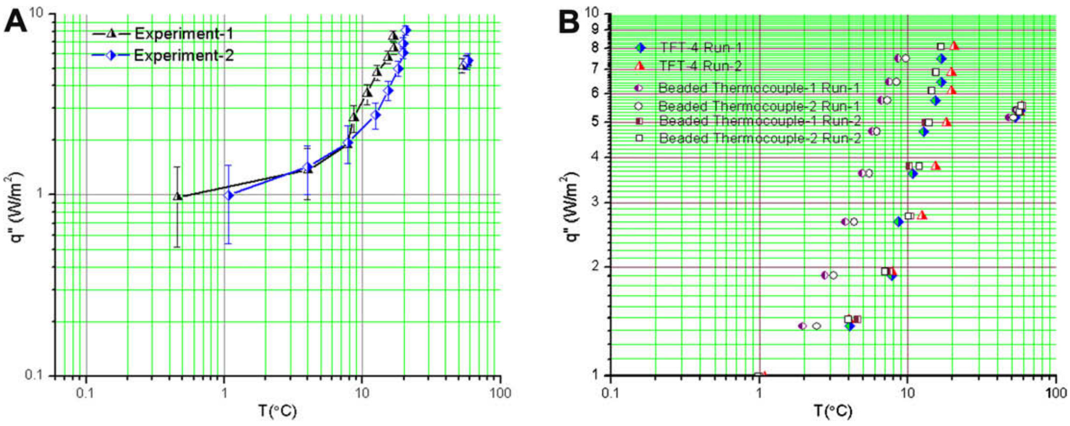

Fig. 3. Pool boiling curves for 10° subcooled case using PF-5060 as the test fluid for two experimental runs. The wall temperature as measured by the (A) TFT and (B) the beaded thermocouples and TFT.

taken after attainment of each steady state condition until the Leidenfrost point is crossed and the vapor film collapses at which point the experimental run is complete. Additional details can be found in [31].

4. Analysis of experimental data

4.1. Determination of heat flux

The heat flux within the copper block is firstly evaluated using the temperature profiles, assuming one-dimensional heat conduction. The copper block is well insulated by air on its sides and by insulating foam located at the base of the viewing chamber below. The high thermal conductivity of copper ensures that the assumption of one-dimensional heat conduction is reasonably valid. Heat fluxes are determined for each of the vertically aligned thermocouples positioned at different depths and radial locations. The mean of all these heat fluxes gives the mean axial heat flux. Fourier's law of one-dimensional heat conduction is used to estimate heat fluxes as follows:

$$\overline{q''_{\mathrm{Cu}}} = \frac{\sum_{i=1}^{n} \frac{k\Delta T_i}{\Delta x_i}}{n} \tag{2}$$

The heat flux on the wafer is determined using the following relation resulting from energy conservation:

$$\overline{q''_w} = \frac{\overline{q''_{\mathrm{Cu}}}}{A_w} A_{\mathrm{Cu}} \tag{3}$$

4.2. Determination of uncertainty in heat flux

The relative uncertainty in heat flux within the copper block is evaluated using the Kline and Mc Clintock [32] procedure. The resulting expression for the relative uncertainty in heat flux within the copper block based on a single pair of vertically aligned thermocouples is:

$$\omega_{q''_{\mathrm{Cu}},i} = \sqrt{\left(\frac{\omega_k}{k}\right)^2 + \left(\frac{\omega_T}{T_j - T_k}\right)^2 + \left(\frac{\omega_{\Delta x}}{\Delta x}\right)^2} \tag{4}$$

The thermal conductivity of copper is taken from the standard tables to be 398 W/mK. The relative uncertainty in the thermal conductivity is ±1%. The relative uncertainty in the positioning of the thermocouples is ±3%. The magnitude of uncertainties in the temperatures T_k and T_j are determined using a 95% confidence and steady state temperature readings. The average error estimates for the heat flux data is given by the following expression:

$$\omega_{\overline{q''_w}} = \frac{1}{n}\sqrt{\sum_{i=1}^{n}\left(\omega_{q''_{\mathrm{Cu}},i}\frac{q''_{\mathrm{Cu},i}}{\overline{q''_{\mathrm{Cu},i}}}\right)^2} \tag{5}$$

The relative uncertainties in wall heat fluxes near CHF are ±6% in both the runs. In film boiling these values are ±9% for both runs.

4.3. The subcooled pool boiling curve

The heat flux within the copper block is evaluated using Eq. (1). The resulting value is used to evaluate the flux from the wafer from (2). The surface temperature is measured by the TFT. The resulting pool boiling curves are plotted in Fig. 3(A) and (B). The heat loss in the radial direction and bottom of the copper block is estimated to be ∼15% in nucleate boiling and ∼40% in film boiling.

4.4. Embedding and evaluation of the correlation dimension

The time-record of the surface temperature obtained from the pool boiling experiments are analyzed. In order to reconstruct the attractor from a single temperature time-series record, the delay-reconstruction technique is used. This approach requires the specification of (i) a suitable delay time and (ii) a suitable embedding dimension.

The mutual information [28] function is used to estimate the optimal delay time for the two-dimensional and three-dimensional cases. Differences in the values of optimal delays for the two-dimensional and three-dimensional cases exist. However, this difference is not very relevant [28] as it is an estimate, to begin with. The two-dimensional delay estimates are used for higher dimensional (up to 15) phase space reconstruction. The TISEAN package contains a simple implementation of the algorithm given in Ref. [28]. In many cases especially at high wall-superheat values, a clear minimum is not obtained. A sophisticated code was obtained from authors of Ref. [28], which refined the grids locally using a chi-squared test. This code results in clear minima for most superheat values. Optimal embedding dimensions are determined using a recurrence plot and false-nearest neighbor tests.

Temperature data at each steady state condition, acquired at 1000 Hz frequency and 1.5 s total time (1500 data points) is used for estimating the correlation dimensions before noise reduction. The correlation dimensions are also estimated using 18,000 data points after noise reduction, to explore the impact of limited data and its impact on the estimate. This is well short of the Tsonis [33] criterion which states that $10^{2+0.4D}$ ($D \sim 11$ in the present case ≈2511,887) points are required for accurate estimation of the correlation dimension. In case of high-dimensional systems, is well in excess of the computational capabilities of most supercomputers. Furthermore, the convergence rate of correlation dimensions is logarithmic [34]. The reconstructed phase spaces are then used to estimate the correlation integral corresponding to different space scales for each dimension [23,24]. The variation of the correlation dimension with the space scale for all dimensions is plotted on a log–log scale for each wall superheat. The slopes of the linear regions of the $\log_{10}C(r)$ vs. $\log_{10}(r)$ graph for each dimension is estimated. The leveling of the slopes provides an estimate of the correlation dimension at that wall superheat.

5. Results and discussion

5.1. Pool boiling results

Fig. 3(A) and (B) depicts the pool boiling curves obtained by plotting the time-averaged surface temperature measured by the TFT (∼200 Hz) and the two beaded thermocouples vs. the spatio-temporally averaged axial heat flux for two experimental runs. Transient temperature measurements from wire-bead thermocouples mounted on the wafer surface are unreliable due to the large junction size resulting in inadequate high frequency response, variations in localized nucleation at the bond site between runs. Additionally, the junction size (∼1 mm in diameter) of the wire-bead thermocouple surrounded by the adhesive is much larger than the thermal boundary layer thickness. Thus, a significant spatial averaging occurs wherein, the temperature reading shown by the wire-bead thermocouple is an average of the surrounding subcooled bulk liquid temperature and the heater temperature. In contrast, the TFT has a thickness of ∼250 nm, which is lesser than the thermal boundary layer thickness. The fidelity of surface temperature readings of the TFT is therefore better.

The surface consists of four packaged TFT of which one stopped functioning during calibration. The first run had three functioning TFT while the second had two functioning TFT. In the first test, TFT-2 consistently shows an averaged temperature reading ∼2.3 °C lower than TFT-3 and the beaded thermocouples. In the second test, TFT-2 (not depicted in Fig. 3) measurements indicate low signal to noise ratios at heating block temperatures exceeding ~140 °C. The high noise component is clear from the Fourier spectra generated in real-time and from the high standard deviations during the heat flux computations (~1.2). Complete failure of the TFT as in the case of TFT-3 in the second run results in a loss of signal in real-time. In case of partial failure such as that of TFT-2, wild excursions (rise or fall) in temperatures by as much as ~7–8 °C are seen following which, the temperature reading settles at a constant lower or higher value until the next excursion occurs. This is indicative of inappropriate contact at the bond site.

The surface temperatures shown by TFT-2 and 3 differ by a maximum of ~8.1 °C near CHF from that shown by TFT-4 in the first run and match closely with the beaded thermocouple readings. TFT-2 shows a maximum difference of ~3.7 °C and ~2.5 °C from the two beaded thermocouple readings in nucleate boiling in the first run. TFT-3 shows a maximum difference of ~1.7 °C and ~1.3 °C, respectively, from the beaded thermocouple readings. However, anomalous excursions in temperature are observed to occur at irregular time-intervals in real-time monitoring of these thermocouples. Therefore, the temperature readings of these thermocouples are not reliable. In the first run, the difference between the beaded thermocouples and TFT-4 wall-superheat values range from a minimum of ~0.75 °C to a maximum of ~9.38 °C near CHF. The value of this difference increases with rise in wall superheat. Correspondingly, for the second run, these differences range from ~-0.57 °C at minimum to ~5.39 °C for TFT-4.

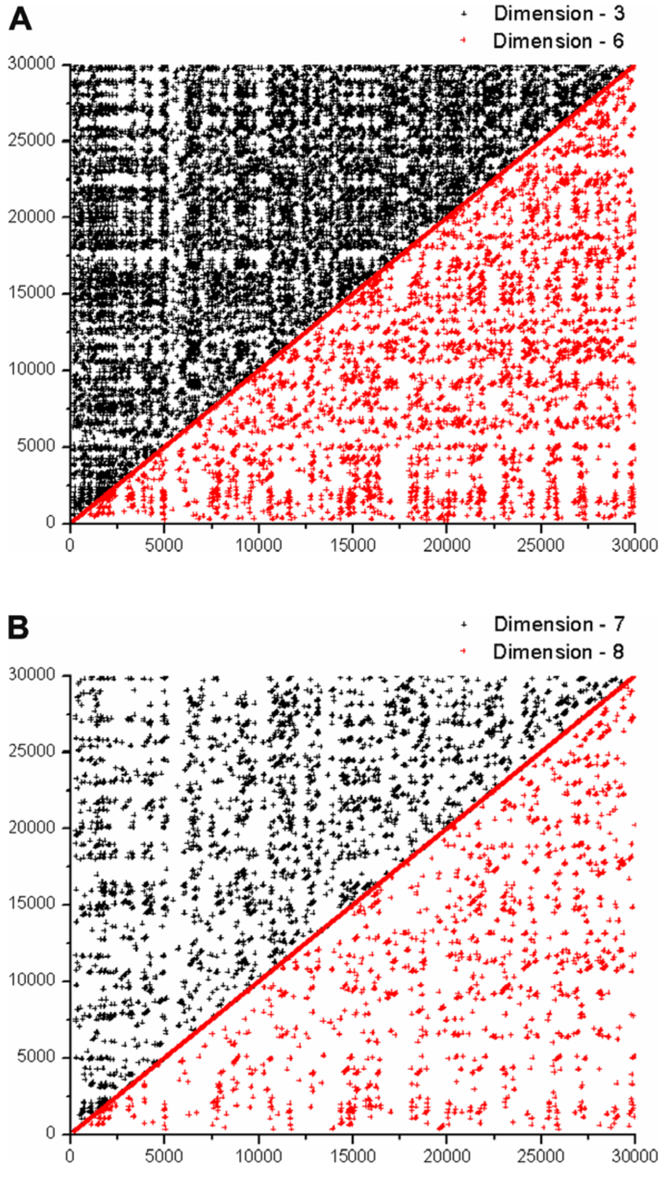

Fig. 4. (A) Recurrence plot near CHF, for the second run, for embedding dimensions of 3 and 6. (B) Recurrence plot near CHF, for the second run, for embedding dimensions of 7 and 8.

Heavy nucleation is observed near the beaded thermocouples due to the presence of adhesive used to attach it (the beaded thermocouple) to the wafer. However, such heavy nucleation is not observed in proximity of the TFT sensing junctions. A temperature difference of ~2–3 °C exists in the vertical direction (~5 cm vertical distance) as determined from the thermocouples submerged in the liquid pool. This leads to the formation of toroidal convection currents within the chamber. This has been experimentally verified using PIV studies in [35]. The formation of convective currents causes additional spatial temperature differential between the periphery and the center accounting for some of the observed temperature differences between the TFT and the beaded thermocouple readings. Additionally, temperature differentials of the order of 2 °C could result between the TFT and the beaded thermocouples due to differences in localized nucleation and convection currents. The remaining difference between readings of TFT-4 and the beaded thermocouples in each run could be due to micro-scale local hot spots forming in vicinity of the TFT sensing junction due to nucleation.

The time-averaged temperature readings of TFT-4 differ by a maximum of about ~0–5.5 °C between the two runs from Fig. 3(A). The time-averaged readings of the wire-bead thermocouples differ by ~1.3–8 °C between the two runs (Fig. 3(B)). In both cases, TFT-4 shows higher averaged wall-superheat values than either of the two beaded thermocouples at all steady state conditions except for one point in the second run. However, both the beaded thermocouples and the TFT show a variation of ~6–8 °C between the two runs indicating that the reliability of the TFT is not an issue and some surface variables are at play.

Earlier studies [36] have shown that significant variations in wall superheats may occur between runs because of aging of the heater surface leading to the deactivation of some cavities. No sign of aging is determined in these experiments from a visual inspection of the test surface. Excursions of ~6 °C in wall superheat between runs are common in the pool boiling literature [5,37]. This aside, small variations in the power supplied to the heaters, subcooling levels (~±0.5 °C) inevitably exist between runs. These in turn lead to variations in active nucleation site densities and hence the surface temperature. These factors could explain the observed difference in surface temperatures recorded by TFT-4 between the two runs. Subsequent tests run under saturation conditions and subcooling levels of 10 °C show a difference of ~2–5 °C in wall superheat between runs.

Fig. 3 shows the pool boiling curves for the two runs. Temperature measurements from TFT-2 have lower signal to noise ratios at higher wall temperatures in the second run and are not shown. The averaged peak heat flux in the first run is ~7.5 W/cm^2. For the second run, the peak heat flux is 8.1 W/cm^2. At wall superheats in excess of 5 °C, significant nucleation is observed, causing an increase in the slope of the boiling curves. At a wall superheat of 8.61 °C, a sudden increase in heat flux results with a small change in wall superheat near TFT-4. This could be due to activation of a nucleation site in close proximity to the thermocouple junction. This does not occur in the second run. Little or no nucleation is visible at wall superheats less than 7 °C. This is because the single crystal silicon wafer is atomically smooth and the highly wetting properties of the test liquid results in a significant barrier to nucleation site activation. The wall heat fluxes in film boiling in the vicinity of the Leidenfrost point is approximately 5.1 W/cm^2 in

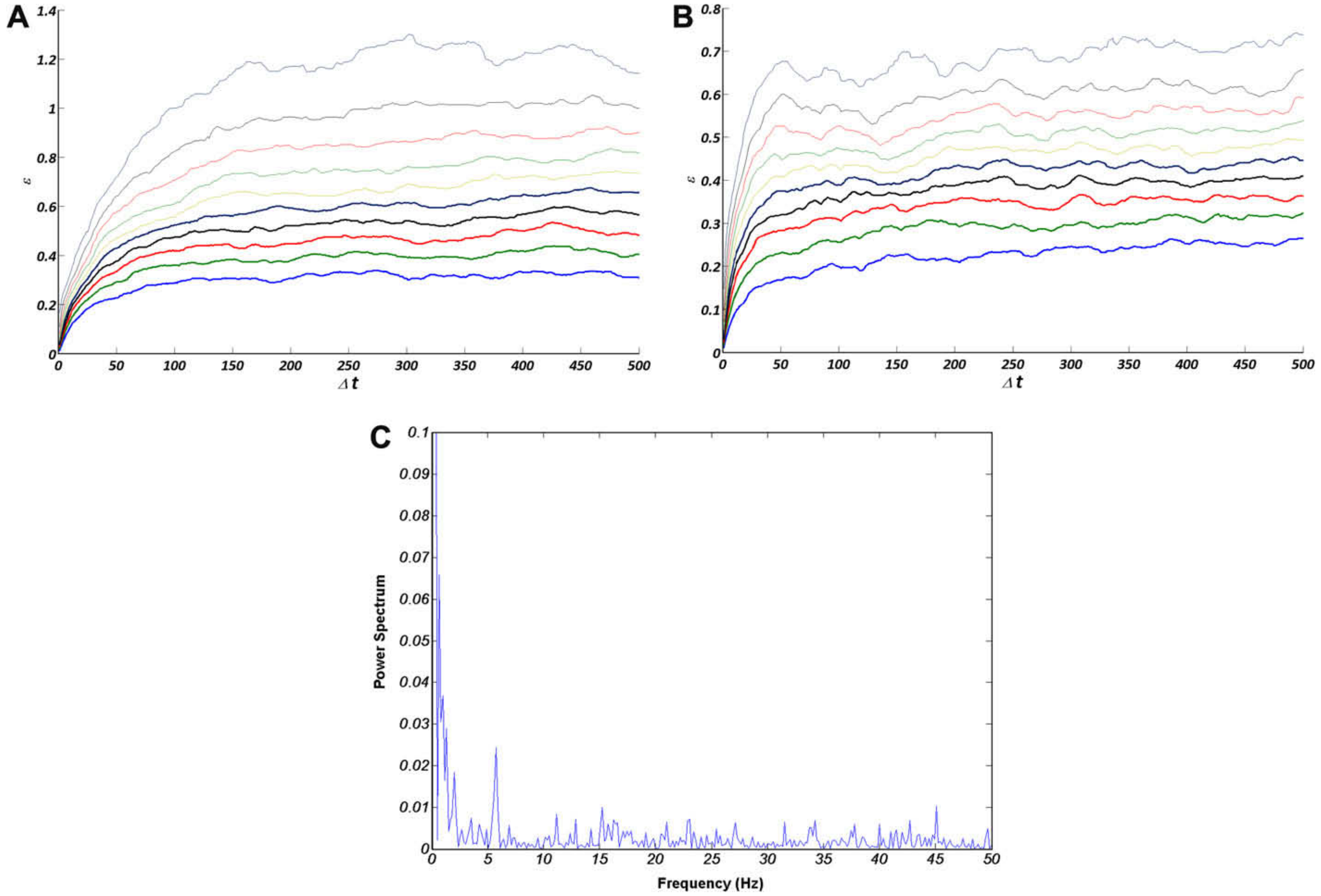

Fig. 5. Space–time separation plots for the second experimental run for an embedding dimension of 10. Contour lines are shown for a spatial separation of ε, for a given temporal separation Δt at different fractions of all pairs. (A) For the CHF condition saturation is seen to occur for $\Delta t > 200$. (B) For the film-boiling condition saturation occurs for $\Delta t > 50$.

the first run and about 5.3 W/cm^2 in the second run which is significantly higher than the value of 3.41 W/cm^2 observed on a bare rectangular silicon wafer at the same levels of subcooling in earlier experiments. Significant disruption of the vapor film occurs due to presence of the connecting wires to the TFT array. Therefore, significantly higher power settings were required to sustain the vapor film as compared to the settings required in previous tests at same subcooling levels conducted on a bare silicon surface.

5.2. Temperature time-series analyses

The quantification of most non-linear statistics with the exception of the calculation of the mutual information function and correlation dimension is done using the freely available TISEAN package.

5.2.1. Recurrence plots

Recurrence plots enable visual identification of suitable embedding dimensions for attractor reconstruction. Trajectories arising from deterministic processes result in recurrences in state-space to the neighborhood of a point through which the trajectory passed before. In case of chaotic attractors, the returns occur in arbitrarily small neighborhoods of the points. The following matrix is evaluated:

$$S_{ij} = U\left(\varepsilon - |\bar{z}_i - \bar{z}_j|\right) \tag{6}$$

If the point i on the trajectory returns to the ε-neighborhood of the point j at a previous time instant, then $S_{ij} = 1$ else $S_{ij} = 0$. Plotting S_{ij} by dots for all recurrences results in a recurrence plot. The plots are interpreted as follows:

(i) If a process is chaotic, a number of short lines parallel to the diagonal will be visible.
(ii) If in addition a number of isolated points are observed, it indicates that the embedding dimension is too low.
(iii) Presence of noise also results in isolated points.

Additional patterns may be observed depending on the dynamics of the system and is a topic of current research. Fig. 4(A) and (B) shows representative recurrence plots at the CHF condition corresponding to the second experimental run. Fig. 4(A) shows that an embedding dimension of three (plotted above the diagonal) is insufficient to unfold the structure of the attractor. An embedding dimension of six (Fig. 4(A) below the diagonal) may reveal some structure but still seems insufficient to unfold the attractor. A large number of isolated points are observed in addition to a number of short lines parallel to the diagonal. Fig. 4(B) shows the recurrence plot for the same case for embedding dimensions of seven and eight. At an embedding dimension of eight, a significant reduction in the number of parallel lines occurs combined with a decrease in the number isolated points. Thus, it seems an embedding dimension of eight or above may be suited to embed the attractor completely. Similar trends are observed for fully developed nucleate boiling and film-boiling points. Suitable embedding dimensions range from 7 to 10 for these cases. For points near onset of nucleate boiling (ONB) and in partial nucleate boiling (PNB), no clear trends

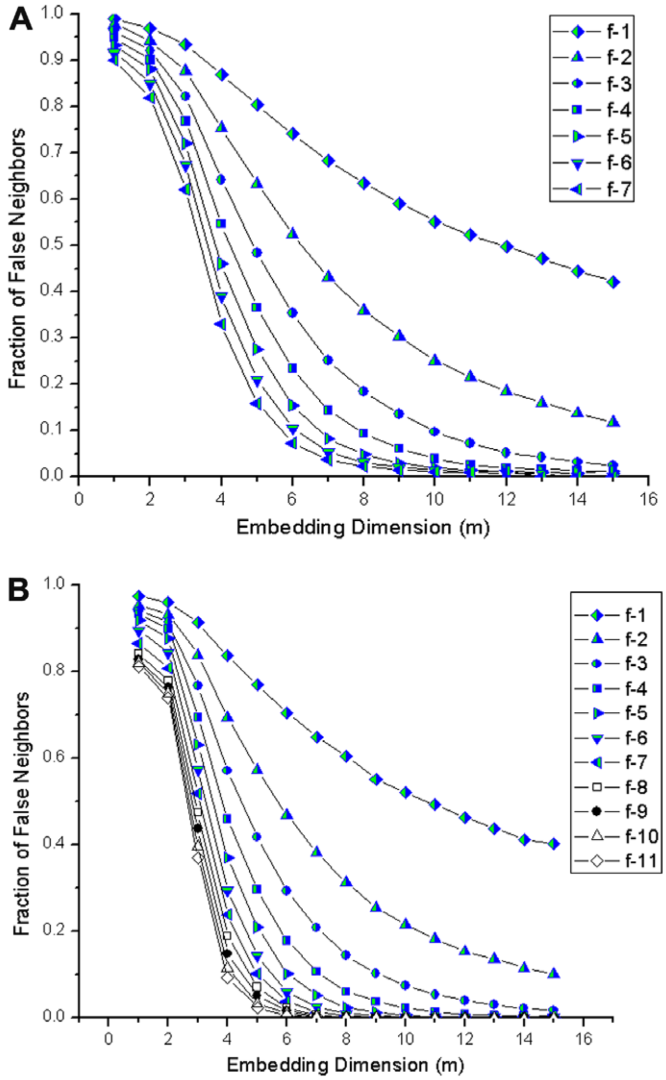

Fig. 6. (A) False-nearest neighbor estimate near CHF for 10 °C subcooling for first run. (B) False-nearest neighbor estimate near CHF for the saturation case.

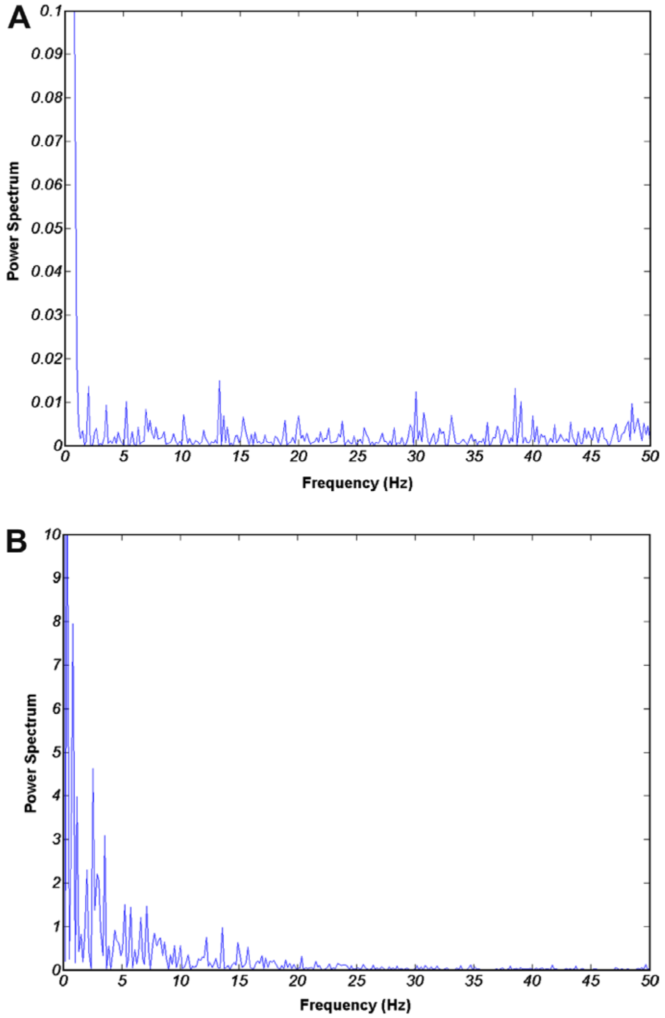

Fig. 7. (A) FFT of beaded thermocouple temperature signals on the wafer surface in film boiling. (B) FFT of TFT (No. 4) temperature signals on the wafer surface in film boiling.

are seen from the recurrence plots indicating that the underlying transport processes may be stochastic, noisy or of very high dimensionality. The concentration of power at lower frequencies (0–2 Hz) is clearly seen in the Fourier spectra and may be indicative of significant noise levels at these wall-superheat values. Non-linearity, if present in these regimes, may be weak.

5.2.2. Space–time separation plots

Presence of long-time temporal correlations in time-series measurements leads to spurious estimates for embedding dimensions using false-nearest neighbor tests and to low dimensional estimates of correlation dimensions of the attractor. The presence of temporal correlations results in 'knees' in plots of correlation dimensions vs. space scale and leads to low dimensional estimates [34].

This bias can be avoided by estimating the temporal correlation duration and eliminating all points within this duration from estimation of dimensions of the attractor. Space–time separation plots aid in indentifying the temporal correlation window. Additionally, it can also be used to identify the presence of noisy or random processes in data. The underlying principle is that, the presence of temporal correlations influences the probability of a pair of points being within a ε-neighborhood of one another. The probability now depends on both the size of the neighborhood and the time elapsed between the two measurements. Saturation or leveling of the curves indicates the absence of temporal correlations and thus the 'Theiler Window'. Lack of saturation in the plots is evidence of stochastic processes. Fig. 5(A) and (B) depicts representative space–time separation plots for the CHF condition and film boiling. Definite saturation is observed for fully, developed nucleate boiling, CHF and film-boiling regimes. For points near ONB and in PNB, no clear saturation is observed indicating the possible dominance of noise. The saturation of space–time curves gives us an estimate of the appropriate Theiler windows to be used for subsequent computations.

5.2.3. False-nearest neighbors

The method of false-nearest neighbors is an elegant method to estimate suitable embedding dimensions. If the correct embedding dimension for an attractor is m_0 and this attractor is projected onto a lower dimension m, certain axes are eliminated by the projection. Points whose co-ordinates are eliminated by the projection differ strongly can become "false neighbors" in the m-dimensional space. Thus, for each point of the time-series, a nearest neighbor search is done in m-dimensions. The ratio of the distances between the two points in m dimensions and $m + 1$ dimensions is computed. If this is larger than a threshold, the neighbor is false.

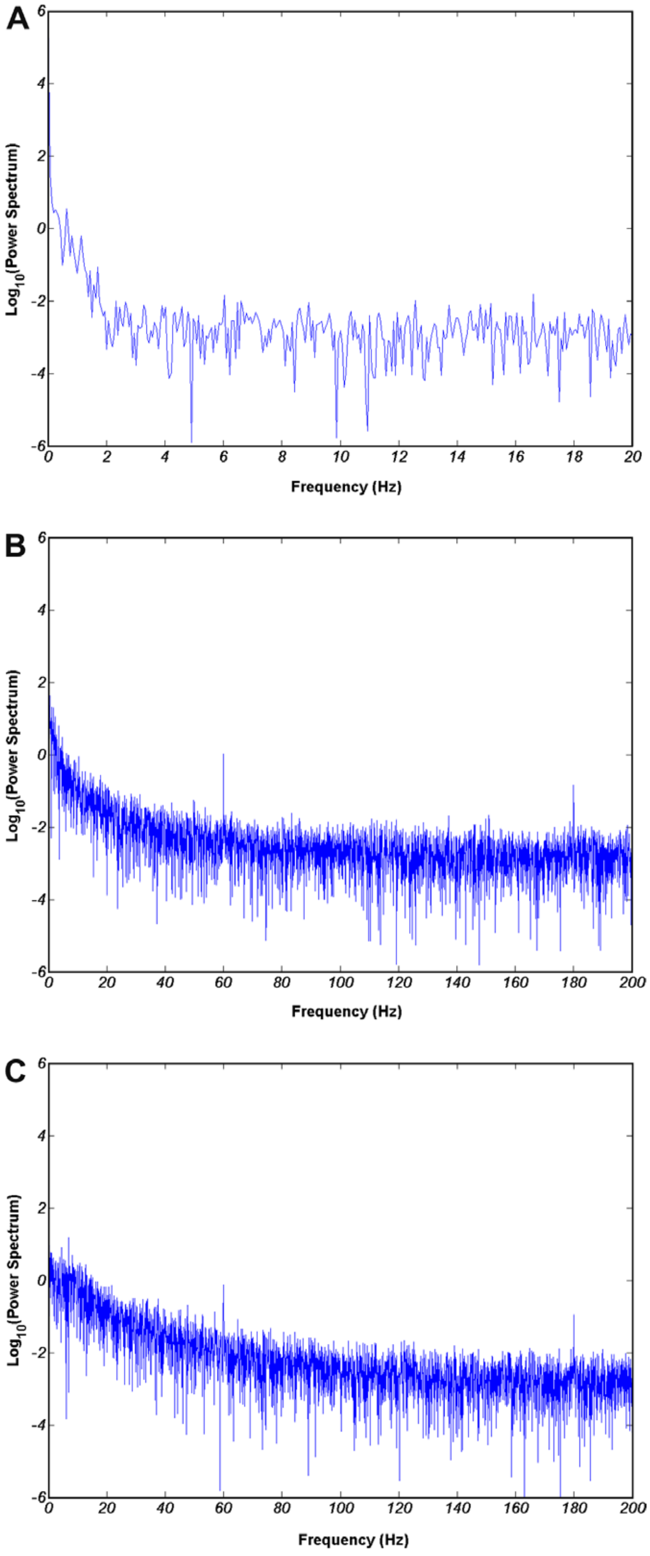

Fig. 8. (A) Semi-log plot of FFT of TFT (No. 4) temperature signals on the wafer surface at $T_w = 56.5$ °C. (B) Semi-log plot of FFT of TFT (No. 4) temperature signals on the wafer surface near CHF ($f = 0$–200 Hz). (C) Semi-log plot of FFT of TFT (No.4) signals on the wafer surface in film boiling ($f = 0$–200 Hz).

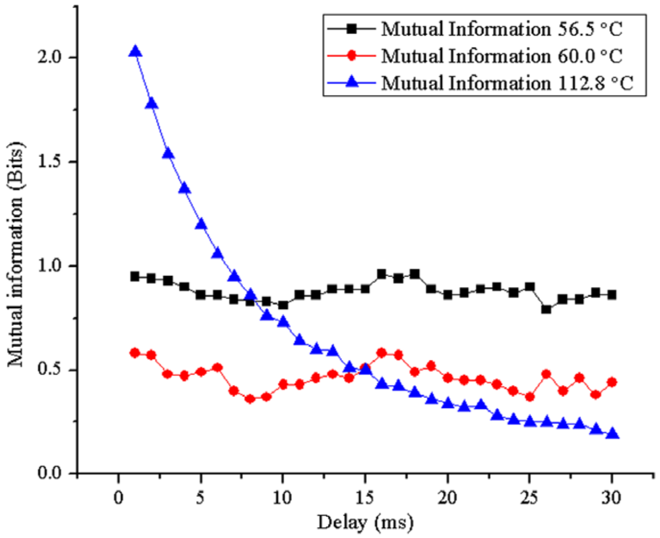

Fig. 9. The variation of mutual information functions with delays for the first experimental run for different boiling regimes. The delay corresponding to the first minimum of the mutual information function is chosen as the value of delay for reconstruction of the higher dimensional phase spaces.

Fig. 6(A) and (B) shows estimates of the false-nearest neighbor fraction for different values of embedding dimension and threshold at CHF for the first experimental run of the 10° subcooled case and a saturation run. Near CHF, the predicted embedding dimension by the false-nearest neighbors test is ~7–9 for the subcooled case and ~5–7 for the saturated case. The corresponding values for film boiling are ~6–7 for the subcooled case and ~5–6 for the saturated case. These observations are consistent with the correlation dimension estimates of 9.1 near CHF and 7.7 in film boiling for the subcooled case.

5.2.4. Power spectra

Fig. 7(A) and (B) shows the plots of the power spectrum vs. frequency (obtained using fast Fourier transforms) for the beaded thermocouple located on the test surface and the TFT in film boiling. The FFT spectrum of the wire-bead thermocouple (Fig. 7(A)) clearly shows its thermal inertia. The power at various frequencies is of the order of ~0.1 or lower. The TFT is more sensitive to surface temperature fluctuations due to its small form factor and the associated lower thermal inertia. This is clearly seen in Fig. 7(B), where the power spectrum is ~10 for frequencies ranging from ~0 to 5 Hz. The onset of chaos usually results in a broadband frequency spectrum.

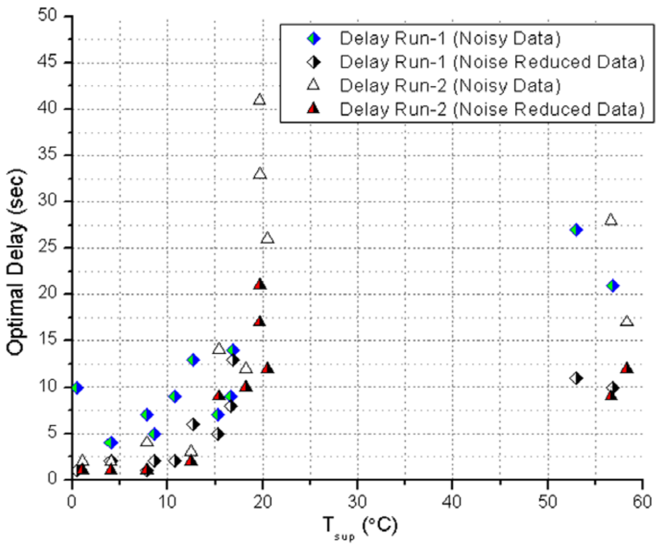

Fig. 10. Variation of optimal delay times with wall superheat.

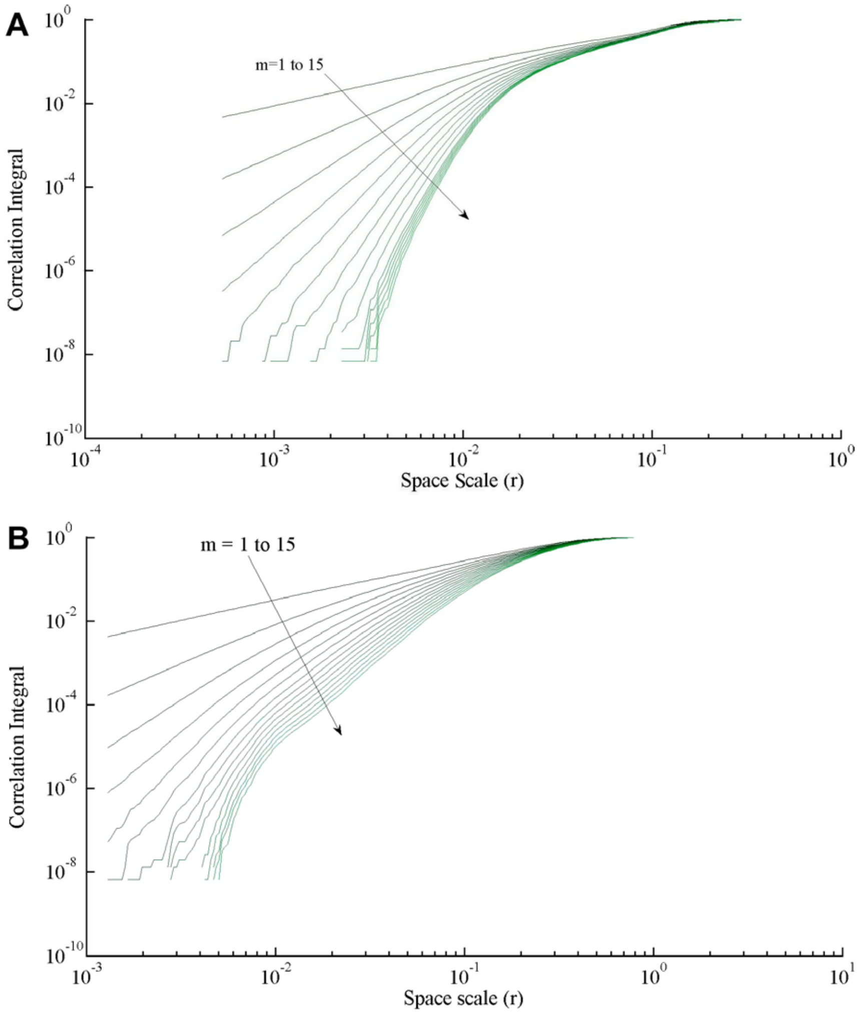

Fig. 11. Variation of correlation integral with space scale after noise reduction, for various embedment dimensions, for nucleate boiling regime, corresponding to the first experimental run for surface temperatures of (A) 56.5 °C and (B) 72.85 °C.

Fig. 8(A)–(C) shows semi-log plots of the power spectrum as a function of the frequency of surface temperature fluctuations – corresponding to different levels of wall superheats. This is clearly seen in Fig. 8(A)–(C). The span of the broadband spectrum increases with an increase in surface temperature. However, other processes (linear and non-linear stochastic) may result in similar spectral responses especially when most of the power is concentrated at the lower end of the frequency spectrum.

As the superheat increases the decay region increases in span. At a wall temperature of ~56.5 °C (Fig. 8(A)) a rapid decay in the power spectrum for frequencies ranging from 0 to 3 Hz is observed, beyond which the observed fluctuations are due to instrumental noise [38,39]. The instrumental noise to signal ratio is $\sim 10^{-2}$ as shown in Fig. 8. The frequency span/bandwidth of the decay region increases with increase in wall temperature (Fig. 8(B) and (C)) and near CHF, it spans a frequency band of ~0-50 Hz. In the film-boiling regime, the decay region (Fig. 8C) spans the frequency band of ~0–100 Hz. An exponential decay in the power spectrum at high frequencies may be an indicator that the system is deterministic and not stochastic where the decay usually obeys a power law [38]. This trend is observed in both the runs.

5.2.5. Correlation dimensions

Prior to estimation of the correlation dimension, the optimal time-delay is estimated for purposes of embedding and generation of higher dimensional phase space vectors. The average mutual information is evaluated from the following expression:

$$I(\tau) = \sum_{T(n),T(n+\tau)} P(T(t), T(t+\tau)) \log_2 \left[\frac{P(T(t), T(t+\tau))}{P(T(t))P(T(t+\tau))} \right] \qquad (8)$$

The point where the mutual information firstly, takes a minimum is used as the optimal value of delay. Fig. 9 depicts the variation of the mutual information function with specified delays for nucleate boiling, CHF condition and the film-boiling regime corresponding to the first experimental run. The first minimum of the mutual information function is used as the optimal delay value for purposes of embedding. Fig. 10 depicts the variation of optimal delays with the wall superheat. The code for mutual information function evaluation is obtained from the authors of Ref. [28]. The delay that corresponds to the first minimum of the mutual information function is chosen as the optimal value for the reconstruction of the phase space using the surface temperature data.

Attractor dimension and Lyapunov exponents are invariants, i.e. their values remain fixed irrespective of the details of the embedding such as delays, measurement function, etc. A fractal dimension coupled with a positive value of Lyapunov exponent indicates the presence of deterministic chaotic dynamics. Therefore, it is important to estimate the correlation dimensions to characterize the dynamics and by extension, the number of active degrees of freedom of the system. The correlation integral is evaluated as follows:

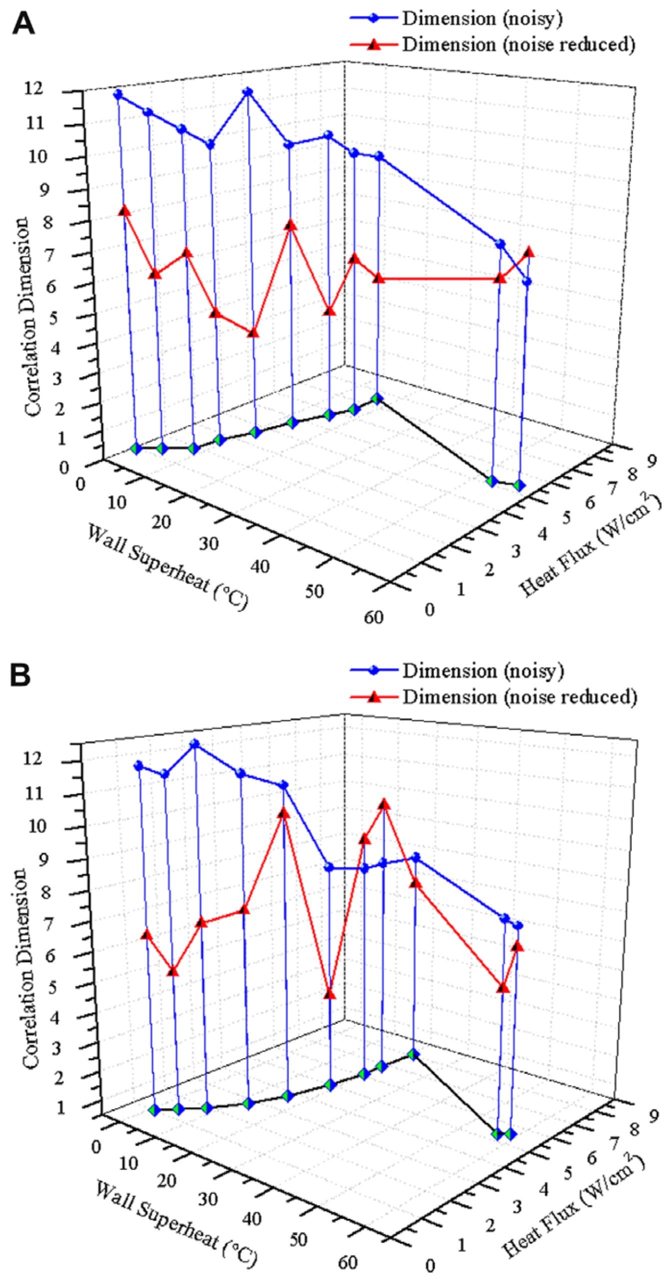

Fig. 12. (A) Variation of correlation dimension in subcooled pool boiling for the first experimental run before and after noise reduction. (B) The variation of correlation dimension in subcooled pool boiling for the second experimental run before and after noise reduction.

$$\widehat{C}(\varepsilon,m)=\frac{1}{m^2}\sum_{j=1}^{m}\sum_{i=1}^{m}U(\varepsilon-|\bar{z}_i-\bar{z}_j|) \tag{9}$$

The correlation dimension is then found as:

$$\nu=\lim_{\varepsilon\to 0}\frac{\ln\widehat{C}(\varepsilon,m)}{\ln\varepsilon} \tag{10}$$

Fig. 11(A) and (B) shows the variation of the correlation integral with the space scale ‘*r*’ for different values of embedding dimensions ‘*d*’ for two nucleate boiling points. The slopes are evaluated from these graphs and used to estimate the correlation dimension. The correlation dimension (Fig. 12(A)) is observed to increase from a value of 11.75 to a peak of 11.81 at the onset of nucleate boiling (ONB) in the first run. This decreases to about 9.05 near CHF in the first run showing that the complexity of the system is reduced under subcooled conditions close to CHF. The corresponding estimates for the second run (Fig. 12(B)) are 7.9 near CHF and between 7.3 and 7.5 in film boiling. It must be noted that the correlation dimension is an estimate and could be influenced by factors such as the number of points used in its computation [27]. The maximum dimensionality ($D_{\max}$) that can be determined from a time-series of length N is:

$$D_{\max}\sim(2\log 10N)-2 \tag{11}$$

For 1500 data points, the maximum value of correlation dimension that can be reliably estimated is ~4–5. In the present case, all correlation dimensions estimates exceed this range suggesting that the attractors of a pool boiling system have a complex geometry. Thus, longer time-series datasets of the order of 10^4 are needed to obtain estimates that are more reliable. This would require sophisticated algorithms employing binary trees. The TISEAN package has an algorithm for determining the correlation dimensions using an optimized neighbor search algorithm and binary trees. This algorithm has been employed on noise-reduced data. The aforementioned correlation dimension estimates are close to the dimension ranges predicted by the recurrence plots and false-nearest neighbor tests. The presence of noise in time-series data results in high-dimensional behavior. From the false-nearest neighbors test, it is clear that the level of experimental noise is ~3% near CHF and in film boiling. From these preliminary correlation dimension estimates, lower values near CHF and fully developed nucleate boiling (FDNB) compared to the nucleate boiling regime, suggest reduced complexity of attractors of the system near CHF. This could be due coalescence of the bubbles leading to formation of vapor columns. Preliminary estimates of Lyapunov spectrum at CHF and in FDNB have one positive value showing that pool boiling is chaotic in these regimes. Thus, theoretical expressions relating peak heat fluxes to liquid thermo-physical properties have been relatively easy to obtain.

From the space–time separation plots, frequency spectra and recurrence plots, noise could be playing a significant role at points near ONB. Additional tests would be required for confirming the presence of non-linear determinism, estimates of correlation dimensions and the validity of assigning a dimension value to pool boiling systems.

In the film-boiling regime the correlation dimensions of the system varies between 7 and 8. This is in contrast to the values of 3–4 obtained in saturated film boiling in Ref. [26]. In that study, the wire dimensions were of the order of the bubble dimensions in the film-boiling regime. Furthermore, high temperature fluctuations of the order of 70 °C were observed. Some differences in the correlation dimension are observed close to CHF (~6.9 for run 1 and ~4.6 for run 2) between the two runs. This could be a result of irreproducibility of the exact power settings to the cartridge heaters or due to differences in noise level. Clear saturation in slopes was observed in these regimes. Further investigations are needed to determine the role of aging of the heater on the statistical estimates.

5.2.6. Phase plots

Phase plots are constructed in three-dimensions for different wall superheats and representative plots for three different wall-superheat values are depicted in Fig. 13(A)–(F). The structure of the attractor is not clearly visible due to incomplete unfolding; nevertheless, some important details can be extracted from the plots. The structure of the attractors near onset of nucleate boiling (Fig. 13(A) and (B)) is similar in structure and elongated for both runs. Furthermore, the attractors near onset of nucleate boiling are very dense compared to those near CHF and in film boiling. This indicates that the attractors near onset of nucleate boiling suffer more strongly due to projection in three dimensions than those

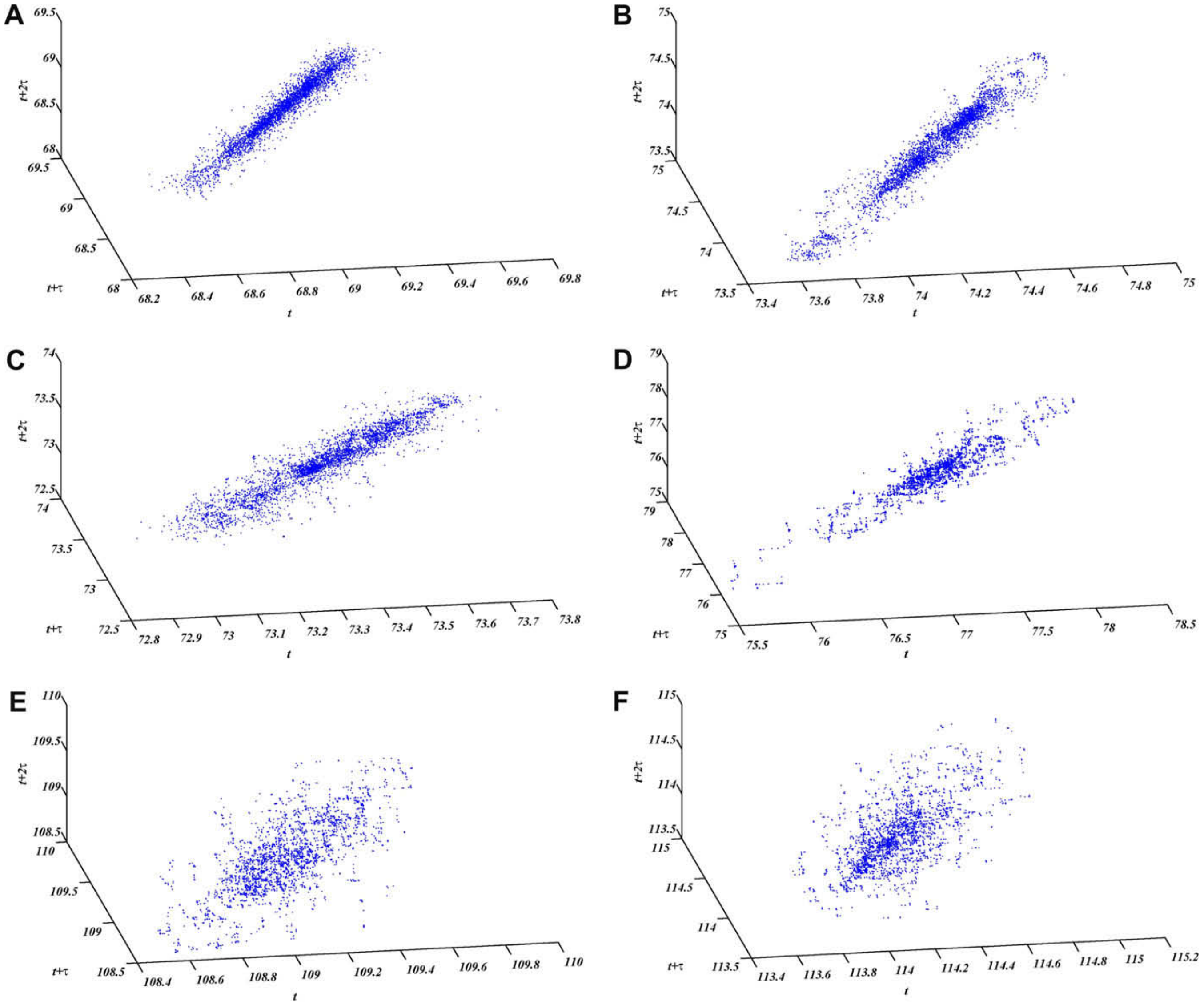

Fig. 13. Phase plots for experimental run 1 (left column) and run 2 (right column) after noise reductions: (A) and (B) partial nucleate boiling, (C) and (D) CHF, and (E) and (F) film boiling.

near CHF and film boiling. This implies that the attractor near onset of nucleate boiling may have a higher dimensionality than that near CHF and film boiling.

Fig. 13(C) and (D) shows phase plots of the attractors near CHF. The CHF point is not attained exactly in these experiments. Slight differences in the power settings can easily cause the pool boiling system to overshoot the CHF leading to film boiling. Due to the inherent, minute irreproducibility in power settings, a difference in the maximum heat flux observed between the two runs is evident. In the first run, the peak heat flux was $\sim 7.5\ \mathrm{W/cm^2}$ and $\sim 8.1\ \mathrm{W/cm^2}$ in the second run. The attractor near CHF in the second run (Fig. 13(D)) shows a simpler structure than the comparatively denser structure of the attractor in the first run. This trend is observed for attractors in fully developed nucleate boiling between the two runs. The correlation dimensions are lower in these regimes for the second run. This is borne out in the phase plots. The reason for this difference is yet unclear.

Fig. 13(E) and (F) depicts the phase plots for the two runs in film boiling. The structure of the attractor is very sparse compared to those near CHF. This indicates that the unfolding is better for these cases further indicative of a lower dimensionality. The lower dimensionality is corroborated by the correlation dimension and false-nearest neighbor computations.

Fig. 14(A) and (B) shows the noise-reduced phase plots at CHF and film boiling for saturated pool boiling. While the attractor (Fig. 14(A)) seems to be denser than those for the subcooled cases at CHF, the converse is true for film boiling. The attractor for saturated film boiling is well unfolded compared to the attractors for subcooled film boiling.

6. Conclusions

Surface temperature transients were recorded during subcooled pool boiling experiments using surface micro-machined thin film thermocouples (TFT). The following trends emerge from the analyses:

1. The pool boiling curves are obtained for both runs. Variations exist in the wall-superheat levels and heat transfer rates between both runs. The dimension of subcooled pool boiling has been explored using recurrence plots, false-nearest neighbor and correlation dimension estimates without and with the application of Theiler Windows, noise reduction.

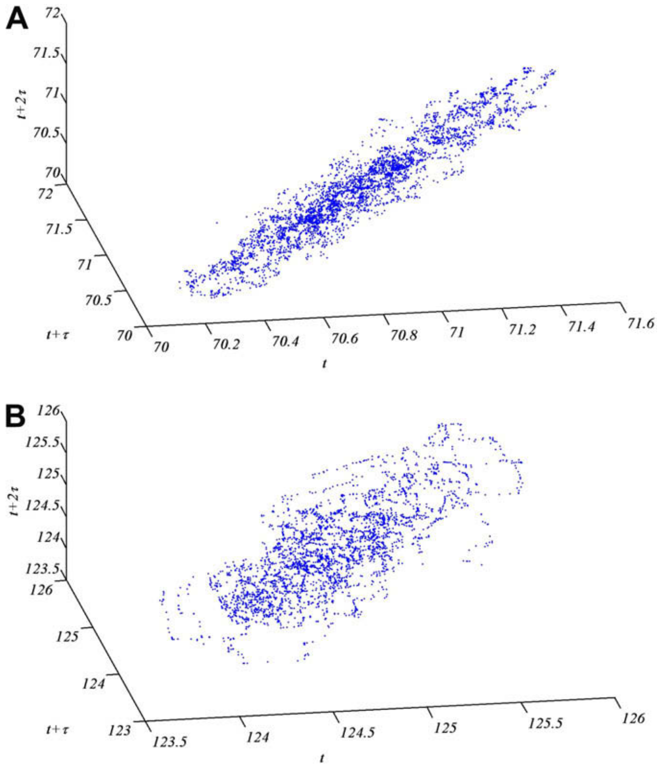

Fig. 14. Phase plots for saturated pool boiling (A) CHF, (B) film boiling.

2. ONB and PNB have high values of correlation dimension. Additionally, the absence of significant number of lines parallel to the diagonal in recurrence plots, the absence of saturation in space–time plots and the higher levels of false neighbors indicated by the false-nearest neighbor tests are indicative of the dominance of noise and/or stochastic transport mechanisms.
3. FDNB is somewhat less complex than PNB. Near CHF, there is a further decrease of the correlation dimension, which shows that the degrees of freedom of the pool boiling system decreases in FDNB compared to PNB. Film boiling is the simplest of all pool boiling regimes and has a correlation dimension of about 6–8. These results are contrary to those obtained in Ref. [26].
4. The estimates show that the number of active degrees of freedom of the pool boiling system changes with the wall superheat and boiling regime.
5. False-nearest neighbor estimates have been compared for CHF and film-boiling conditions for saturated and subcooled pool boiling. The estimates show that saturated pool boiling has fewer active degrees of freedom than subcooled pool boiling.
6. Positive values of Lyapunov exponents and fractal dimensions of the reconstructed attractor show that FDNB, CHF and film boiling have chaotic dynamics.
7. Preliminary analyses of the Fourier spectrum seem to show a quasi-periodic transition from a periodic or possibly multiply periodic state to a chaotic state. Further analysis of the spectrum is currently in progress
8. Phase plots are generated for the original dataset and the noise-reduced datasets for saturated pool boiling (CHF, film boiling) and subcooled pool boiling. The phase plots for the original data show a wool-ball shaped attractor. Thus, the attractor geometry is not clearly visible. In contrast, the noise-reduced attractors show well-defined structures that vary with wall-superheat levels.

References

[1] V.K. Dhir, Boiling heat transfer, Annu. Rev. Fluid Mech. 30 (1998) 365–401.
[2] Issam Mudawar, Assessment of high-heat-flux thermal management schemes, IEEE Trans. Compon. Packag. 24 (2) (2001) 122–141.
[3] E.I. Nesis, Boiling of liquids, Sov. Phys. Uspekhi 8 (1966) 883–907.
[4] P. Sadasivan, C. Unal, R. Nelson, Perspective: issues in CHF modeling – the need for new experiments, Trans. ASME 117 (1995) 558–567.
[5] V.P. Carey, Liquid–Vapor Phase-Change Phenomena, first ed., Taylor & Francis, Washington, DC, 1992. pp. 222–245.
[6] M. Buchholz, H. Auracher, T. Lüttich, W. Marquardt, Experimental investigation of local processes in pool boiling along the entire boiling curve, Int. J. Heat Fluid Flow 25 (2) (2003) 243–261.
[7] T. Lüttich, W. Marquardt, M. Buchholz, H. Auracher, Identification of unifying heat transfer mechanisms along the entire boiling curve, Int. J. Therm. Sci. 45 (2006) 284–298.
[8] J.G. Myers, V.K. Yerramilli, S.W. Hussey, G.F. Yee, J. Kim, Time and space resolved wall temperature and heat flux measurements during nucleate boiling with constant heat flux conditions, In. J. Heat Mass Transfer 48 (2005) 2429–2442.
[9] L. Harris, E.A. Johnson, The technique of sputtering sensitive thermocouples, Rev. Sci. Instrum. 5 (4) (1934) 153–158.
[10] R. Marshall, L. Atlas, T. Putner, The preparation and performance of thin film thermocouples, J. Sci. Instrum. 43 (1966) 144–149.
[11] L.H. Bullis, Vacuum-deposited thin-film thermocouples for accurate measurement of substrate surface temperature, J. Sci. Instrum. 40 (12) (1963) 592–593.
[12] D.N. Assanis, F.A. Friedmann, A thin film thermocouple for transient heat transfer measurements in ceramic coated combustion chambers, Int. Commun. Heat Mass Transfer 20 (1993) 458–468.
[13] D. Debey, R. Bluhm, N. Habets, H. Kurz, Fabrication of planar thermocouples for real-time measurements of temperature profiles in polymer melts, Sensors Actuators A 58 (1997) 179–184.
[14] X. Tian, F.E. Kennedy, J.J. Deacutis, A.K. Henning, The development and use of thin film thermocouples for contact temperature measurement, Tribol. Trans. 35 (1992) 491–499.
[15] M. Laugier, The construction and use of thin film thermocouples for the measurement of surface temperature: applications to substrate temperature determination and thermal bending of a cantilevered plate during film deposition, Thin Solid Films 67 (2004) 163–170.
[16] N. Sinha, Design, fabrication, packaging and testing of thin film thermocouples for boiling studies, M.S. Thesis, Texas A&M University, College Station, Texas, 2006.
[17] H.-S. Ahn, V. Sathyamurthi, S. Lau, D. Banerjee, Boiling experiments using vertically aligned carbon nanotubes and using surface micromachined thin-film thermocouples (TFT), AIAA 2006–2916, in: Proceedings of the 9th Joint AIAA/ASME Thermophysics and Heat Transfer Conference, San Francisco, CA, 2006.
[18] M. Shoji, Studies of boiling chaos: a review, In. J. Heat Mass Transfer 47 (2004) 1105–1128.
[19] R. Mosdorf, M. Shoji, Chaos in nucleate boiling-non-linear analysis and modeling, In. J. Heat Mass Transfer 47 (2004) 1515–1524.
[20] N. Acharya, M. Sen, E. Ramos, Periodicity and bifurcations in capillary tube boiling with a concentric heating wire, In. J. Heat Mass Transfer 46 (2003) 1425–1442.
[21] L. Zhang, M. Shoji, Nucleation site interaction in pool boiling on the artificial surface, In. J. Heat Mass Transfer 46 (2003) 513–522.
[22] H.-O. Peitgen, H. Jürgens, D. Saupe, Chaos and Fractals, second ed., Springer, New York, 2004. pp. 605–713.
[23] A. Ben-Mizrachi, I. Procaccia, P. Grassberger, Characterization of experimental (noisy) attractors, Phys. Rev. A 29 (2) (1984) 975–977.
[24] P. Grassberger, I. Procaccia, Characterization of strange attractors, Phys. Rev. Lett. 50 (5) (1983) 346–349.
[25] F. Takens, Detecting strange attractors in turbulence, in: D.A. Rand, L.-S. Young (Eds.), Lecture Notes in Mathematics 898, Springer, Berlin, 1988, pp. 366–381.
[26] M. Shoji, T. Kohno, N. Negishi, S. Toyoshima, A. Maeda, Chaos in Boiling on a small-size heater, in: Proceedings of ASME-JSME Thermal Engineering Joint Conference, vol. 2, 1995, pp. 233–238.
[27] H. Kantz, T. Schreiber, Nonlinear Time Series Analysis, second ed., Cambridge University Press, New York, 2005. pp. 31–46.
[28] A.M. Fraser, H.L. Swinney, Independent coordinates for strange attractors from mutual information, Phys. Rev. A 33 (2) (1986) 1134–1140.
[29] K.G. Kreider, D.C. Ripple, D.P. DeWitt, Calibration of thin film thermocouples on silicon wafers. Available from: <http://www.cstl.nist.gov/nist836/836.05/papers/Kreider00TConWafer_Calibration.pdf>.
[30] S. Bhavnani, G. Fournelle, R.C. Jaeger, Immersion-cooled heat sinks for electronics: insight from high-speed photography, IEEE Trans. Compon. Packag. 24 (2) (2001) 166–176.
[31] V. Sathyamurthi, H.-S. Ahn, D. Banerjee, S.C. Lau, Subcooled pool boiling experiments on horizontal heaters coated with carbon nanotubes, J. Heat Transfer 131 (2009) 071501-1–071501-10.
[32] S.J. Kline, F.A. Mc Clintock, Describing uncertainties in single-sample experiments, Mech. Eng. 75 (1953) 3–8.
[33] C. Sprott, Topics in physics: chaos and time-series analysis, Fall 2000, http://sprott.physics.wisc.edu/phys505/.

[34] J. Theiler, Estimating fractal dimension, J. Opt. Soc. Am. A 7 (6) (1990) 1055–1073.
[35] D. Banerjee, V.K. Dhir, Study of subcooled film boiling on a horizontal disc. Part 2. Experiments, J. Heat Transfer 123 (2001) 285–293.
[36] C. Corty, A.S. Foust, Surface variables in nucleate boiling, in: Chemical Engineering Progress Symposium Series, vol. 51, 1955, pp. 1–12.
[37] A.K. Das, P.K. Das, P. Saha, Nucleate boiling of water from plain and structured surfaces, Exp. Therm. Fluid Sci. 31 (2007) 967–977.
[38] A. Brandstater, H.L. Swinney, Strange attractors in weakly turbulent Couette–Taylor flow, Phys. Rev. A 35 (5) (1987) 2207–2221.
[39] D. Sigeti, W. Horsthemke, High-frequency power spectra for systems subject to noise, Phys. Rev. A 35 (5) (1987) 2276–2282.